Anal Bioanal Chem (2013) 405:6259–6269
DOI 10.1007/s00216-013-7058-z

RESEARCH PAPER

Advanced surface characterization of silver nanocluster segregation in Ag–TiCN bioactive coatings by RBS, GDOES, and ARXPS

R. Escobar Galindo · N. K. Manninen · C. Palacio · S. Carvalho

Received: 4 March 2013 / Revised: 7 May 2013 / Accepted: 8 May 2013 / Published online: 31 May 2013

Abstract Surface modification by means of wear protective and antibacterial coatings represents, nowadays, a crucial challenge in the biomaterials field in order to enhance the lifetime of bio-devices. It is possible to tailor the properties of the material by using an appropriate combination of high wear resistance (e.g., nitride or carbide coatings) and biocide agents (e.g., noble metals as silver) to fulfill its final application. This behavior is controlled at last by the outmost surface of the coating. Therefore, the analytical characterization of these new materials requires high-resolution analytical techniques able to provide information about surface and depth composition down to the nanometric level. Among these techniques are Rutherford backscattering spectrometry (RBS), glow discharge optical emission spectroscopy (GDOES), and angle resolved X-ray photoelectron spectroscopy (ARXPS). In this work, we present a comparative RBS–GDOES–ARXPS study of the surface characterization of Ag–TiCN coatings with Ag/Ti atomic ratios varying from 0 to 1.49, deposited at room temperature and 200 °C. RBS analysis allowed a precise quantification of the silver content along the coating with a non-uniform Ag depth distribution for the samples with higher Ag content. GDOES surface profiling revealed that the samples with higher Ag content as well as the samples deposited at 200 °C showed an ultrathin (1–10 nm) Ag-rich layer on the coating surface followed by a silver depletion zone (20–30 nm), being the thickness of both layers enhanced with Ag content and deposition temperature. ARXPS analysis confirmed these observations after applying general algorithm involving regularization in addition to singular value decomposition techniques to obtain the concentration depth profiles. Finally, ARXPS measurements were used to provide further information on the surface morphology of the samples obtaining an excellent agreement with SEM observations when a growth model of silver islands with a height d=1.5 nm and coverage θ=0.20 was applied to the sample with Ag/Ti=1.49 and deposited at room temperature.

Keywords Ag–TiCN · Surface characterization · SEM · RBS · GDOES · ARXPS

R. Escobar Galindo (✉)
Instituto de Ciencia de Materiales de Madrid (ICMM–CSIC), Cantoblanco, 28049 Madrid, Spain
e-mail: rescobar@icmm.csic.es

N. K. Manninen · S. Carvalho
GRF–CFUM, Physics Department, University of Minho, Campus of Azurém, 4800-058 Guimarães, Portugal

N. K. Manninen · S. Carvalho
SEG–CEMUC, Department of Mechanical Engineering, University of Coimbra, Rua Luís Reis Santos, 3030 788 Coimbra, Portugal

C. Palacio
Departamento de Física Aplicada (CXII), Universidad Autónoma de Madrid, Cantoblanco, 28049 Madrid, Spain

Introduction

The strategy of surface modification using coatings has proved to offer unique chemical and physical properties able to improve the biological response of biomaterials as well as the wear and corrosion resistance of the base material. The development of new functional coatings, namely DLC [1, 2], TiN [3, 4], TiCN [4], TiAlN [5], and TiSiCON [6, 7] among others, has enhanced the functional properties of different biomaterials. Moreover, the addition of Ag to wear protective coatings reduces the friction coefficient and the wear rate of transition metal nitrides and carbides [8, 9]. The addition of Ag nanoclusters has been also pointed as an effective solution

to reduce bacterial colonization on biomaterials surface, thus enhancing the lifetime of the bio-device [8, 10–15]. The antibacterial activity of silver is attributed to the release of ionized Ag^+, which is claimed to cause the disruption of cell membrane and DNA damage [16]. The efficiency of Ag is mainly controlled by the morphology of silver particles (being known that the smaller particles are more effective in destroying the bacteria) [17, 18] and the interaction between the Ag particles and the electrolyte, which is mainly controlled by the amount of Ag clusters on the coating surface and the morphology of the matrix [11, 19]. Hence, the ultimate bioactive performance of the coatings will be driven by the outmost surface (<10 nm) in contact with the biological environment and high-resolution analytical techniques are needed to complete the characterization. Rutherford backscattering spectrometry (RBS), glow discharge optical emission spectroscopy (GDOES), and angle resolved X-ray photoelectron spectroscopy (ARXPS) are techniques able to provide information about surface and depth composition down to the nanometric level [20].

The co-deposition of transition metal nitrides (MeN) and carbides (MeC) provokes the formation of nanostructured coatings where Ag nanoclusters are dispersed through the base matrix, forming Ag clusters which size increases at higher silver contents [9, 11, 21]. Several authors have reported that silver clusters are able to diffuse in the base coating, which leads to a non-uniform Ag distribution along the coating thickness. Krzanowski et al. [22] produced SiC–Ag and HfC–Ag coatings by magnetron sputtering, and the authors found that, although the Ag particles were embedded in the matrix near the substrate, there was a silver depleted region followed by a surface-rich Ag layer. Adochite et al. [23] found that the co-deposition of Ag and TiO_2 coatings resulted in a non-uniform chemical composition along the thickness, being determined that the silver content was higher near the substrate and lower at the coating surface which was ascribed to diffusion of this element during the deposition process itself. The segregation of Ag to coating surface after annealing was also reported by several authors, who proposed the use of self-lubricant films based on hard coatings combined with a ductile and lubricant Ag phase [9, 24, 25]. In fact, the surface segregation of Ag in different coatings is claimed to be a dynamic process that occurs even at room temperature [26]. Bates Jr. et al. [26] found that the co-deposition of Ag–Si led to the surface segregation of Ag, which was attributed to the immiscibility of Ag and Si. The authors stated that the large surface and strain energies of Ag precipitates in the silicon matrix could further exclude the silver particles from the Si. Manninen et al. [21] performed previous studies in the Ag–TiCN system concluding that the coatings are composed by TiCN, a-C and a-CN_x phases, and crystalline Ag phases, being the size of the Ag grains and the presence of amorphous phases enhanced at higher silver contents. The tribological tests of these coatings were performed in bovine serum solution against an alumina counterpart in order to simulate the environment found in hip joints [8]. The results obtained indicated that the wear resistance of the coatings was enhanced for Ag/Ti ratios lower than 0.20 (Ag content below 6 at.%), while for higher silver contents the wear rate increased. Moreover, the cytotoxicity tests revealed that the mortality rate in MTS assay with fibroblasts was inferior to 10 % for Ag/Ti <1, while for the coating with higher Ag content (27 at.%) the mortality rate increased to 20 %, still being an acceptable result. The results found in previous studies were encouraging indicating that Ag–TiCN coatings are a suitable option as wear protective coatings for hip implants.

Despite of these numerous and excellent works, the mechanism of silver surface segregation and its effect on the bioactivity of the coatings is still not fully understood. The purpose of this paper is, by the use of advanced surface characterization techniques, to shed light on the role of silver nanoclusters at the nanometer scale. In particular, this report aims to obtain a detailed characterization of the Ag composition profile along the depth as well as metal nanocluster size distribution at the surface as function of silver content (from 0 to 27 at.%) and deposition temperature (room temperature and 200 °C) for coatings prepared by reactive magnetron sputtering. As previously mentioned, the size distribution and amount of Ag clusters on the coating surface exert a strong influence on the tribological and biological behavior of these coatings. In this sense, the optimization of this system requires a deep knowledge of the surface properties of Ag–TiCN (i.e., Ag particle size and surface coverage) in order to obtain an effective bioactive coating.

Experimental details

Ag–TiCN coatings were deposited by reactive DC magnetron sputtering both onto polished and ultrasonically cleaned 316L stainless steel (20×20 mm^2) and single crystalline silicon (100) substrates. A pure titanium interlayer was deposited in order to improve the adhesion. A high-purity Ti target (200×100 mm^2) and a mixed Ti/Ag target (200×100 mm^2) were used in a $Ar+C_2H_2+N_2$ atmosphere, with the substrates rotating at 70 mm over the target at a constant speed of 7 rpm. Two series of samples were deposited using a Ti target with 6 and 14 Ag nuggets, resulting in relative Ag sputtering areas (only the preferential eroded zone of the target is considered) of 15 % (first series) and 43 % (second series), respectively. Argon flow was kept constant at 60 sccm while the reactive gases fluxes (C_2H_2 and N_2) were changed. Further details concerning the deposition parameters can be seen elsewhere [21]. The variation in the reactive gas fluxes was performed in

order to maintain approximately constant the C and the N contents, although the current density applied to the targets was changed in order to obtain coatings with different Ag/Ti ratios, ranging from 0 to 1.49. The deposition was carried at a constant voltage of −70 V. The base pressure in the deposition chamber was about 10^{-3} Pa and rose up to values between 3.1×10^{-1} and 4.7×10^{-1} Pa during the deposition. Two series of samples were deposited at different temperatures: room temperature (RT) and 200 °C.

Ball crater test was used to determine the coatings thickness. The coatings chemical composition was determined by electron probe microanalysis (EPMA) in a Cameca SX 50 apparatus. The coating's morphology was evaluated by scanning electron microscopy (EDAX—Nova nanoSEM200) operating at 15 kV in backscattered electron (BSE) mode.

In order to analyze the chemical composition depth profiles of the coatings, Rutherford backscattering spectroscopy (RBS) and glow discharge optical emission spectroscopy (GDOES) were carried out. RBS experiments were performed at the 5MV HVEE Tandetron accelerator sited at the Centro de Micro-Análisis de Materiales of Universidad Autónoma de Madrid [27]. The RBS experiments were performed using 3.7 MeV He^+ ions to make use of the resonance $^{14}N(\alpha,\alpha)^{14}N$ in order to improve the sensitivity to nitrogen. The data were acquired simultaneously with two silicon surface barrier detectors located at scattering angles of 170° and 135°, respectively, with an energy resolution of 16 keV at an ion dose of 10 μC. The experimental spectra were fitted with the software programs RBX [28] and SIMRA [29]. GDOES depth profile analysis of the coatings was completed using a Horiba Jobin Yvon RF GD Profiler equipped with a 4-mm-diameter copper anode and operating in argon gas [30, 31]. In previous works [32, 33], Escobar Galindo et al. performed a complete optimization of the operating conditions for the analysis using this GDOES system. By applying a radiofrequency discharge pressure of 650 Pa and a forward power of 40 W, multilayers in the nanometer range were able to be analyzed. Therefore, in this study these operation settings have been kept fixed. The setup was calibrated using standard materials of known composition. In order to improve the quantification of nitrogen, a series of nitride coatings deposited by magnetron sputtering was used as calibration samples [34]. The emission responses from the excited sputtered elements were detected with a polychromator of focal length of 500 mm. The optical path of the spectrometer is nitrogen purged. The emission lines used were 130.217 nm for oxygen, 149.262 nm for nitrogen, 156.14 nm for carbon, 365.35 nm for titanium, 328.08 nm for silver, 271.441 nm for iron, 341.477 for nickel, and 425.433 nm for chromium. The chamber was cleaned by sputtering a silicon (100) sample for 20 min prior to the measurements. This procedure minimizes the contamination of the samples from the source, allowing a faster stabilization of the plasma and, therefore, a higher surface resolution of the GDOES setup [20]. No memory effects were observed after this pre-sputtering procedure. The uncertainties of GDOES measurements were estimated of 10 % in the thickness and of lower than ±5 at.% in the silver concentration.

The electron spectroscopy measurements were performed in an ultra-high vacuum (UHV) system at a base pressure better than 8×10^{-8} Pa. The XPS spectra were measured using a hemispherical analyzer (SPECS Phoibos 100 MCD-5). The pass energy was 9 eV, giving a constant resolution of 0.9 eV. The Au $4f_{7/2}$, Ag $3d_{5/2}$, and Cu $2p_{3/2}$ lines of reference samples at 84.0, 368.3, and 932.7 eV, respectively, were used to calibrate binding energies. A twin anode (Mg and Al) X-ray source was operated at a constant power of 300 W using Mg K_α (1,253.4 eV) radiation. The analyzed area, which is controlled by the entrance slit of the analyzer, is a circle of around 3.5 mm in diameter. In addition to that, the samples were placed in a sample stage with four degrees of freedom in such a way that the angle between the axis of the input lens of the analyzer and the surface normal could be varied between 0° and 70° in order to perform angle-resolved measurements.

Results and discussion

Chemical composition and morphology of Ag–TiCN coatings

As mentioned above, we have previously reported [21] a complete description of the deposition parameters, chemical bulk composition, and structural characterization of Ag–TiCN coatings deposited at room temperature. The deposition rate and the variations in the chemical composition were found to be mainly controlled by the increase in the current density applied to the targets and the reactive gas flow. According to the chemical composition obtained by EPMA, it was found that the Ag content increased from 0 to 27 at.% along with a decrease in the Ti content from 37 at.% to 18 at.%. The C and N contents were almost constant for the studied samples. Taking into account that the variations in Ag content were accomplished by reducing the Ti content, the coatings were labeled according to their Ag/Ti atomic ratios. For this paper, we have selected four samples with different Ag/Ti ratios (0, 0.2, 0.4, and 1.49) and prepared at room temperature and at 200 °C. In Table 1, a summary of the Ag/Ti ratios, Ag contents, and deposition rates is shown. The coatings deposition rate varies from 1.1 to 1.8 μm/h with the silver content, being clear that the deposition rates are similar for both temperatures.

Figure 1 shows the plain view BSE micrographs of the coatings with different Ag/Ti atomic ratios deposited at RT (left) and 200 °C (right). The distributions of diameters, median of the cluster diameter distribution, and standard deviation of the log-normal fit are also presented for samples Ag/Ti=0.40

Table 1 Silver content, thickness of deposited samples, and results from SEM images analysis

Ag/Ti ratio	Ag content (at.%)	Thickness (μm)		Ag surface area (%)		Ag average diameter (nm)	
		RT	200 °C	RT	200 °C	RT	200 °C
0	0	2.9	2.5	0.00	0.00	–	–
0.20	6	1.4	1.4	0.00	0.00	–	–
0.40	11	3.0	3.0	0.10±0.05	0.50±0.20	24±6	26±6
1.49	27	3.2	3.1	13±1	15±2	30±7	54±25

and 1.49 either deposited at RT and 200 °C, and the data are summarized in Table 1. The BSE imaging mode allows obtaining the elemental contrast of Ag, which appears brighter in the dark TiCN matrix due to its higher atomic mass. From the BSE micrographs of the samples Ag/Ti=0.40 and 1.49, it can be found that Ag nanoclusters are embedded in the TiCN matrix. Since silver is immiscible in TiCN matrix, the deposition of Ag–TiCN coatings results in the formation of nanocomposites with silver nanoparticles embedded in the TiCN matrix. The presence of metallic silver as well as the formation of crystalline TiCN phases was previously confirmed by means of XRD and XPS analysis, and the results can be found elsewhere [21]. However, since the backscattered electrons are produced at high depths (about 1 μm) we cannot infer that the Ag clusters are formed at the outmost surface of the coatings.

Regarding the sample with Ag/Ti=0.20, the presence of Ag clusters was not detected in SEM analysis for the coatings

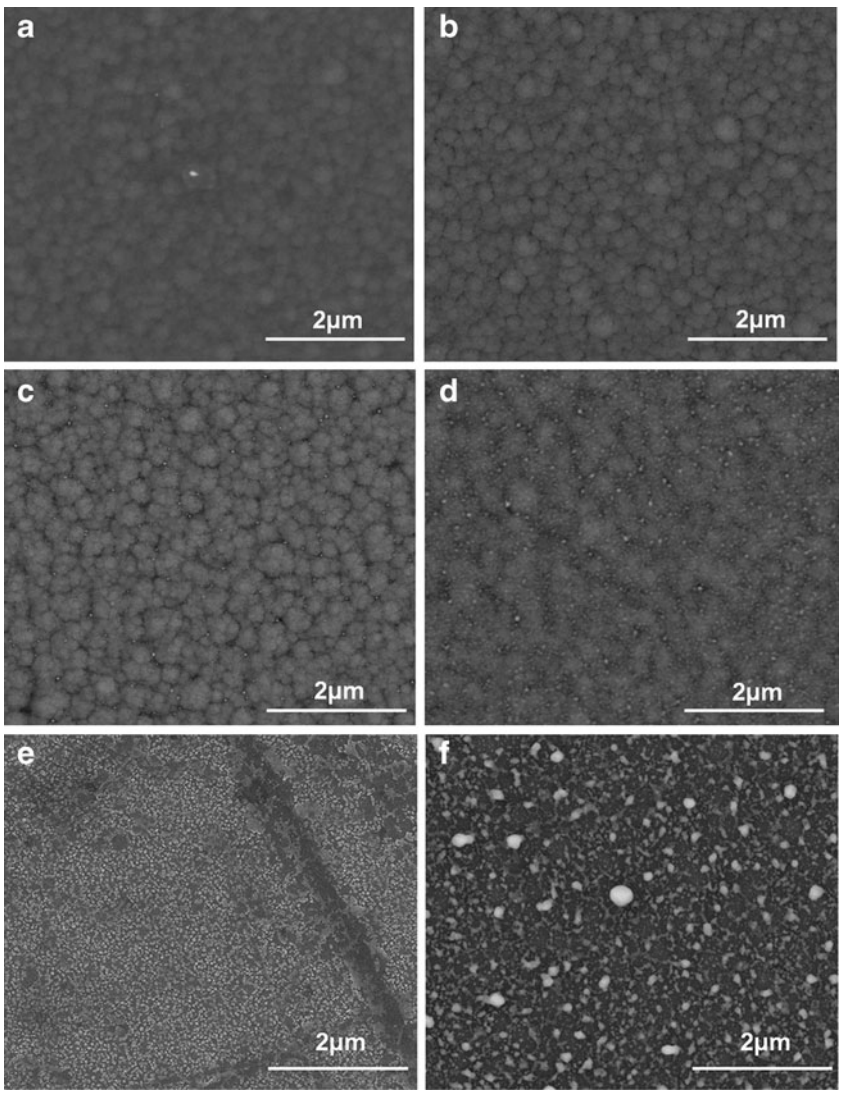

Fig. 1 SEM micrographs: **a** Ag/Ti = 0.2, RT; **b** Ag/Ti = 0.2, 200 °C; **c** Ag/Ti = 0.4, RT; **d** Ag/Ti = 0.4, 200 °C; **e** Ag/Ti = 1.49, RT; and **f** Ag/Ti = 1.49, 200 °C

deposited at RT and 200 °C (Fig. 1a, b), which is plausible due to their small size. The increase of Ag/Ti to 0.40 resulted in the segregation of small Ag clusters to the column boundaries as shown in Fig. 1c for the sample deposited at RT. The average size of the Ag clusters is 24±6 nm (see histogram in Fig. 2a). Increasing the Ag content on the coatings (Ag/Ti=1.49) results in the formation of larger clusters (with an average size of 30±7 nm as presented in Fig. 2c) due to the coalescence during the growth process (Fig. 1e). The increase of Ag clusters size with Ag content was previously reported by several authors [21, 35]. Deposition of the films at higher temperature (200 °C) led to the increase of Ag cluster size up to 26±6 and 54±25 nm for the samples with Ag/Ti = 0.40 and 1.49, respectively, as observed in Fig. 1d (see histogram in Fig. 2b) and 1f (see histogram in Fig. 2d). This effect is attributed to the higher Ag mobility promoted by the temperature increase, being the effect more pronounced for the samples with the highest Ag content (Ag/Ti = 1.49). Liu et al. [36] reported that the co-deposition of Ag–Si at 20 °C and 200 °C led to the formation of Ag nanoclusters embedded in the Si matrix, and the nanocomposite films deposited at 200 °C tend to grow large and well-separated Ag particles while the films deposited at room temperature grow finer Ag particles and their clusters.

In the first section, we have summarized the chemical composition and the morphology of AgTiCN coatings deposited with different Ag/Ti ratios and at two different temperatures (room temperature and 200 °C). Due to the depth resolution of EPMA (about 2 μm), the chemical composition thereby obtained is related only to the bulk of the coating. In the same direction, the BSE imaging mode of SEM, although allowing to unambiguously detect the formation of silver clusters, cannot be used to conclude that they are formed at the surface of the coatings. Therefore, in the following sections we will make use of surface techniques (RBS, GDOES, and ARXPS) to obtain, on the one hand, the compositional depth profiles of the coatings ("Compositional RBS and GDOES depth profiles of AgTiCN coatings") and, on the other, precise information of the segregation of silver on the surface of the coatings as a function of the silver content and deposition temperature ("Ag surface depth profile and segregation").

Compositional RBS and GDOES depth profiles of AgTiCN coatings

Firstly, we have made use of RBS and GDOES as tools to obtain the compositional depth profiles of all the AgTiCN samples deposited at the different Ag/Ti ratios and deposition temperatures. As an example, the RBS spectra and the GDOES composition depth profile of the sample with Ag/Ti=1.49 (deposited at 200 °C) are presented in Fig. 3a and b, respectively.

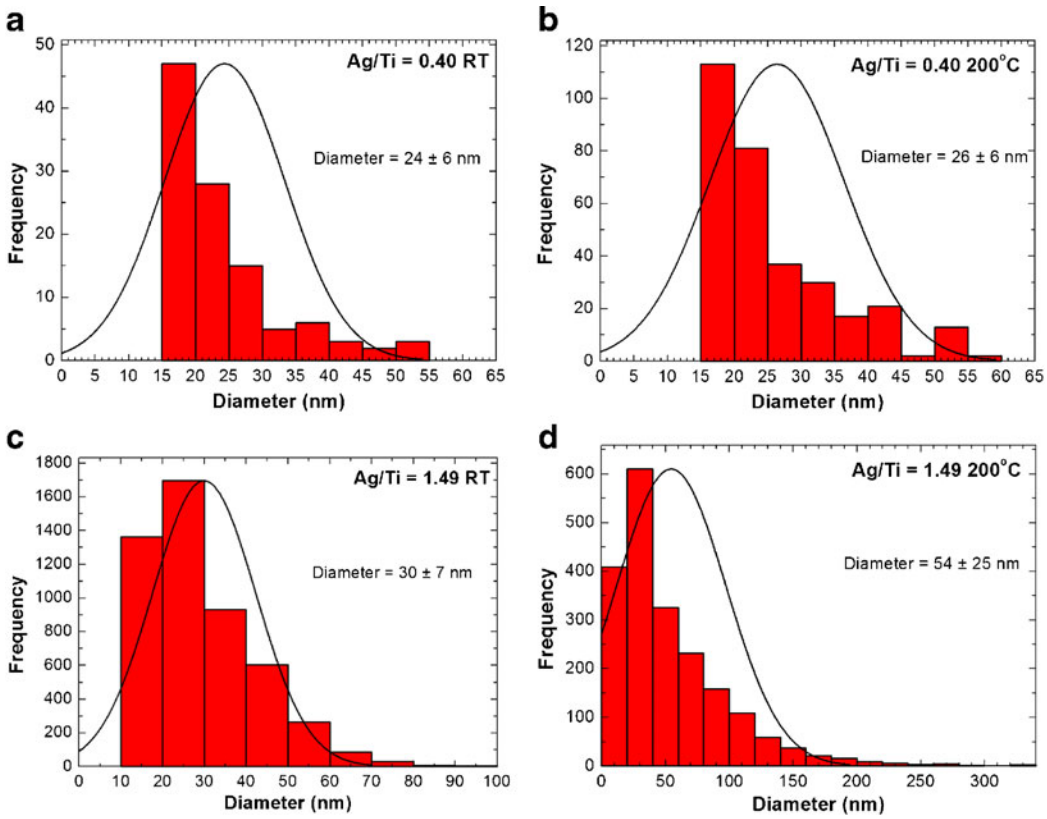

Fig. 2 Histograms of silver cluster diameter for **a** Ag/Ti = 0.4, RT; **b** Ag/Ti = 0.4, 200 °C; **c** Ag/Ti = 1.49, RT; and **d** Ag/Ti = 1.49, 200 °C samples

For clarity purposes, the RBS experimental data and the global fitting of results were shifted vertically from the contributions of the elemental spectra (lower part of the graphs) in Fig. 3a. RBS fitting of the experimental results gave very good agreement once we used a multilayer stack to describe the sample. At the surface, there is a very thin layer of about 170×10^{15} at cm^{-2} with a high content of Ag (up to 30 at.%). Below this surface layer, there is a thin AgTiCN layer of about 910×10^{15} at cm^{-2} with a lower composition of Ag (15–18 at.%) than the bulk AgTiCN coating (20–25 at.%) that was fitted to have 15×10^{18} at cm^{-2}. All those layers showed a very well-defined multilayer coating structure with sharp interfaces down to the limit of the technique (i.e., 5–10 nm). Similar multilayer fitting was applied to the rest of the deposited coatings and they will be discussed in detailed to elucidate the silver surface segregation in the coatings (see "Ag surface depth profile and segregation").

With respect to the GDOES depth profile (Fig. 3b), it can be observed how the elemental composition is very homogeneous within the bulk deposited coating (i.e., thickness above 100 nm) until reaching the Ti interlayer. However, in the inset of Fig. 3b, it can be found that in the first 50 nm the Ti, N, and C contents increase, along with a decrease in the Ag content. In fact, the Ag content decreases from 31 at.% to 15 at.% in the first 20 nm and aftermost it increases to 21 at.% showing a constant value after the first 100 nm until the titanium interlayer is reached at about 3 μm, in excellent agreement with RBS measurements.

Therefore, both RBS and GDOES analysis are consistent with the quantitative chemical composition obtained by EPMA for the bulk coating. However, they provide richer information regarding the compositional depth profile of the films. In particular, it was found that on the surface of the coatings there is a non-homogenous chemical composition. In "Ag surface depth profile and segregation", we will focus on the silver depth profile at the surface of the coatings in order to study the evolution of the silver surface segregation for the different silver contents and temperatures.

Ag surface depth profile and segregation

In Fig. 4a and b, we show a zoom of the RBS spectra of the different coatings deposited at RT and 200 °C, respectively. The range of selected RBS energies allows comparing the segregation of silver in the different deposited samples. The surface Ag is detected in RBS at a typical energy of 3,190 keV and with decreasing energy along the sample depth due to the energy loss of He^+ ions. In addition, the surface titanium signal appears at energy of 2,660 keV for all the studied samples.

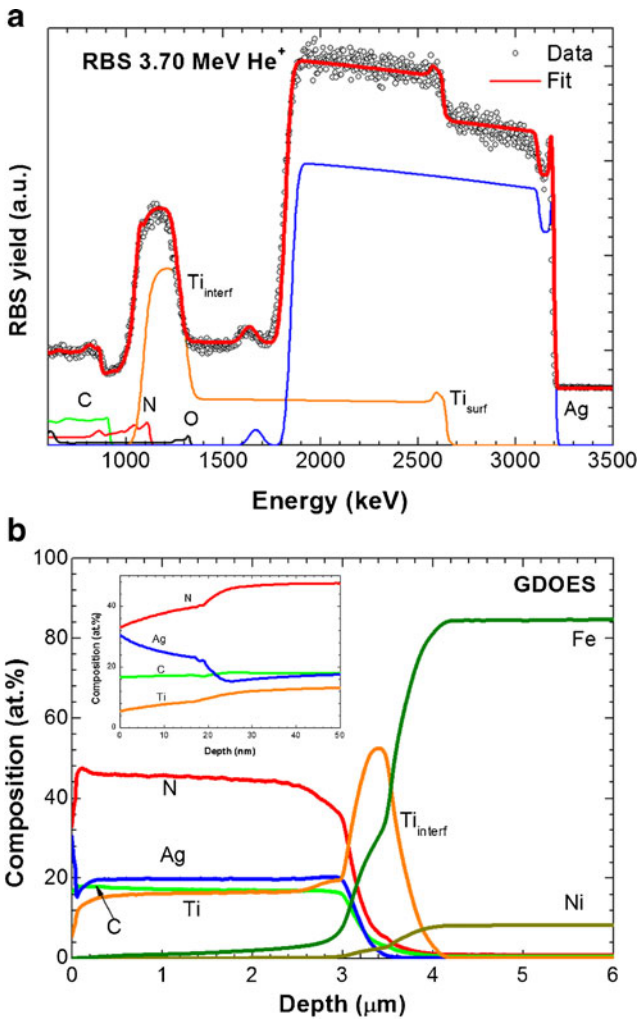

Fig. 3 RBS spectra (**a**) and GDOES depth profile (**b**) of sample Ag/Ti = 1.49 deposited at 200 °C. The inset in (**b**) shows a zoom of the first 50 nm of the GDOES profile

According to the results, it can be found that for samples with Ag/Ti=1.49 there is a very thin top surface layer with a high silver content (zone 1) in the schematic representation of Fig. 4b followed by a silver depletion zone (zone 2) before reaching the silver content of the bulk coating (zone 3). For the sample deposited at room temperature, RBX and SIMRA simulations asses the areal density of the top Ag layer and the depletion zone to be of 40 and 400×10^{15} at cm^{-2}, respectively. In the case of the Ag/Ti=1.49 sample deposited at 200 °C, those areal densities were estimated to be of 170 and 910×10^{15} at cm^{-2} for the top silver layer and the silver depletion zone, respectively. Therefore, it can be observed that an increase of the deposition temperature provoked a surface modification of the AgTiCN that extends two to three times in depth as compared to the sample deposited at room temperature (assuming that there is no substantial change in the density of the films upon deposition at temperature). With respect to the samples prepared with lower Ag/Ti ratio (0.20

and 0.40), the RBS spectra of both samples deposited at RT and 200 °C did not reveal any silver surface segregation.

In order to evaluate more accurately this silver surface segregation effect in the coatings, we have made use of the higher depth resolution at the surface provided by GDOES depth profile analysis. In fact, GDOES has a monolayer resolution at the surface and no worse than 1 nm for the first 100 nm, while RBS shows a depth resolution of 5–10 nm [20]. GDOES depth profiles of the samples are presented in Fig. 5a and b for all the coatings deposited at RT and 200 °C, respectively.

From Fig. 5a, it can be found that the Ag content of the coating with Ag/Ti=1.49 decreases from 46 at.% to 12 at.% along the first 5 nm, after which it increases again reaching a constant value of 21 at.% along the coating thickness. This is consistent with the RBS results that predicted a top layer with high silver content and a subsequent silver depletion zone. On the contrary, no silver segregation was observed for samples Ag/Ti=0.40 and 0.20. It is worth noting that the GDOES results obtained for the coating with Ag/Ti=0.40 show an increase from 0 at.% to 12 at.% in the first 13 nm of the film. The absence of Ag in the surface of this particular coating (corroborated by ARXPS as explained below) confirms that the silver precipitates present in the SEM image of Fig. 1c can be observed because we are using the BSE imaging mode and not because there is any surface segregation. Regarding the samples deposited at 200 °C all the GDOES profiles show a clear silver surface segregation promoted by diffusion process, followed by a silver depletion zone. Moreover, it is found that after this decrease the Ag content increases again to a constant silver bulk concentration. We have located the different interfaces (1—silver top layer, 2—silver depletion layer, and 3—depth where the silver bulk composition is attained) according to the generally used (50/50 %) definition given by Hofmann [37]. As an example, in Fig. 5a we indicated the different layers for the sample deposited at room temperature with Ag/Ti=1.49. In Table 2, the thicknesses of the layers for the different deposited samples are summarized.

The thickness of the silver top layer increases from 3 nm for the sample with Ag/Ti=0.20 up to 18 and 22 nm for samples with ratios of 0.4 and 1.49, respectively. The thickness of the depletion zone varies accordingly with the Ag content. For sample Ag/Ti=0.20, the depletion zone is as thin as 3 nm reaching a constant Ag bulk content of 4–5 at.% before the first 10 nm of depth. The depletion zone extends to higher depths with the Ag content as can be observed in the inset of Fig. 5b showing the silver depth profile along the first ≈20 nm of samples Ag/Ti=0.40 and 1.49. For sample with ratio 0.4, the thickness of the depletion zone was measured to be of 10 nm reaching a constant bulk Ag content of 12–13 at.% after the first 40 nm of depth. Of particular interest is sample with the highest Ag content

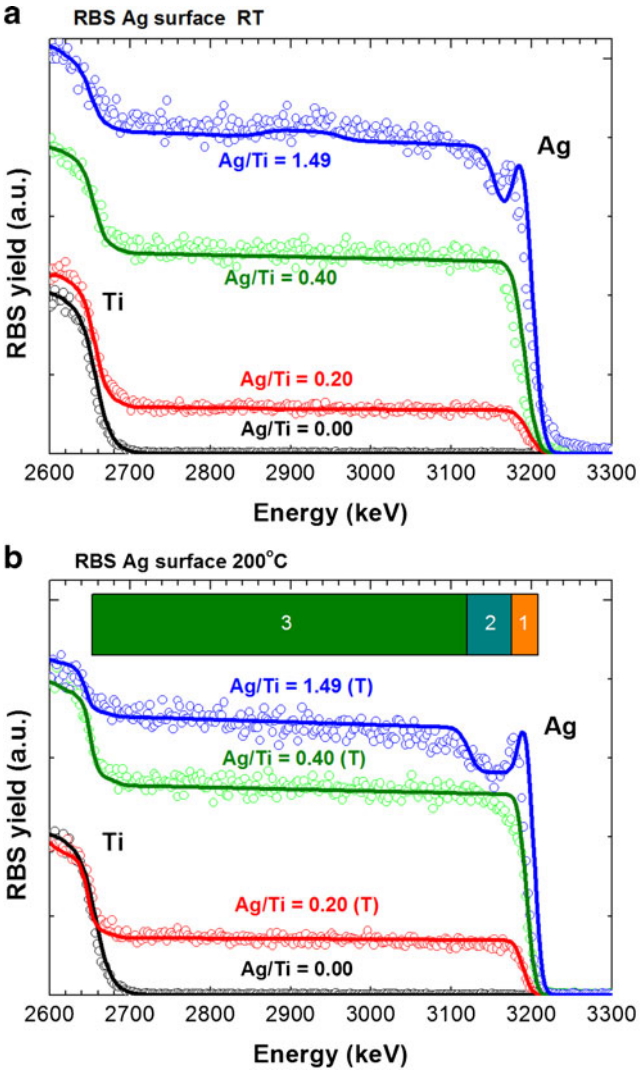

Fig. 4 RBS spectra of samples deposited **a** at RT and **b** at 200 °C. Both graphs are in the same vertical scale. In (**b**), a schematic representation of the different silver regions (*1* silver top layer, *2* silver depletion zone, *3* silver bulk value) is depicted

(Ag/Ti=1.49) where a thickness of 30 nm was measured for the depletion zone, but the bulk Ag content of 20–22 at% was not reached until a depth of 150 nm typical of a diffusion-driven process (see Fig. 6).

The results obtained indicate that, regardless the deposition temperature, coatings with a silver content above a certain threshold (>20 at.% in our case) show an Ag-rich layer on the coating surface below which a Ag depletion zone of few nanometers is formed. Similar results were obtained for all samples deposited at 200 °C even for very low silver contents, being the thickness of the formed layers dependent on the silver composition. Krzanowski et al. [22] also found an Ag-surface-rich layer followed by a depletion zone; however, the thickness of the depletion zone was almost half of the coating thickness (about 500 nm). The surface segregation of Ag was

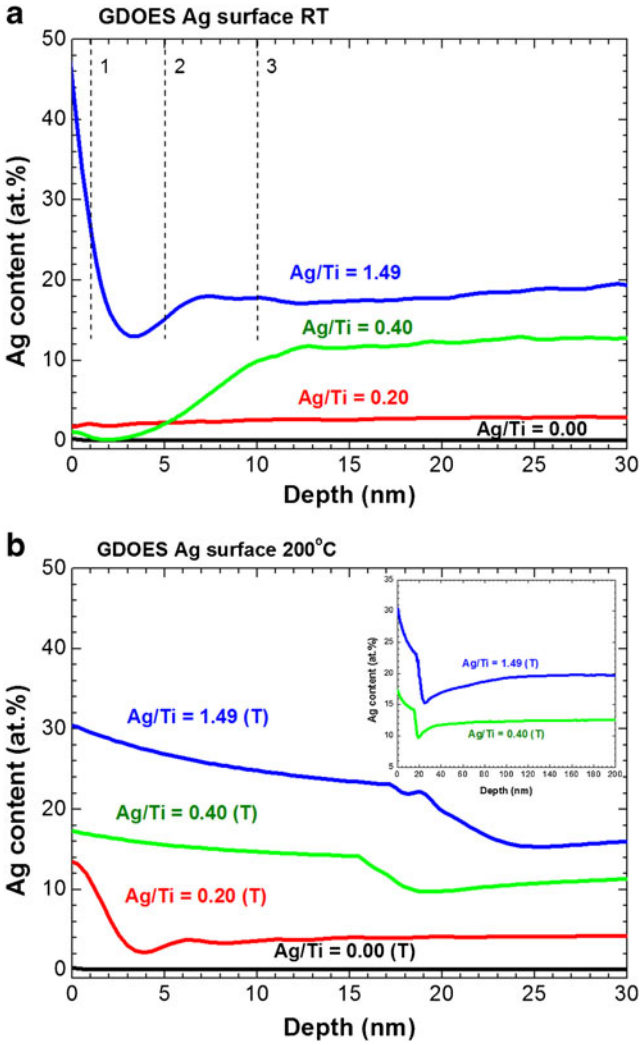

Fig. 5 Ag depth profile near surface (<30 nm) for the coatings deposited at **a** RT and **b** 200 °C. The inset in (**b**) shows the extended depth profiles up to 200 nm for samples Ag/Ti = 0.40 (200 °C) and Ag/Ti = 1.49 (200 °C)

previously reported by several authors [22, 24–26], and it is claimed that this process is driven by the decrease in the surface energy and strain energy associated with the Ag surface segregation [22, 24]. Both the increase in the deposition temperature [26] and annealing treatments [24] are able to activate the diffusion process. In fact, from the results obtained it seems clear that the segregation process depend on the Ag content and deposition temperature, being enhanced with these parameters.

In order to get further information on the near surface composition and morphology, ARXPS measurements were carried out. Figure 7a shows the measured Ag concentrations as a function of the emission angle for samples with different Ag/Ti ratios [Ag/Ti = 1.49 (RT), Ag/Ti = 0.2 (200 °C), Ag/Ti = 0.4 (RT), and Ag/Ti = 0], samples which are those where significant variations of the Ag near surface concentration were found using GDOES. It is worth noting that silver surface

Table 2 Thicknesses of the silver surface layer, depletion layer, and bulk depth measured from GDOES depth profiles for AgTiCN coatings

Sample	Ag top surface (nm)		Ag depletion (nm)		Ag bulk depth (nm)	
	RT	200 °C	RT	200 °C	RT	200 °C
0.2	–	3	–	3	–	10
0.4	–	18	–	10	–	40
1.49	1	22	5	30	10	150

The error in the thickness was estimated to be of 10 %

segregation was found for samples Ag/Ti=1.49 (RT) and Ag/Ti=0.2 (200 °C) but not for sample Ag/Ti=0.4 (RT) in complete concordance with GDOES results. Ag concentrations have been calculated from the signal intensities using the sensitivity factors provided by the manufacturer [38]. It is well known that if XPS spectra are recorded at different emission angles φ, the photoelectron escape depth, $\lambda \cos\theta$ (being λ the attenuation length of emitted photoelectrons), can be varied in such a way that the depth analyzed is changed and therefore the set of angular measurements will contain information on the concentration depth profile of each species. In our case, the intensity of emitted photoelectrons corresponding to the Ag 3d XPS band is given by Eq. (1)

$$I_{\mathrm{Ag}}(\varphi) = \frac{I^{0}_{\mathrm{Ag}}}{\lambda_{\mathrm{Ag}} cos\phi} \int_{0}^{\infty} c_{\mathrm{Ag}}(z) exp\left(\frac{-z}{\lambda_{\mathrm{Ag}} cos\phi}\right) dz \qquad (1)$$

where $c_{\mathrm{Ag}}(z)$ is the Ag concentration at a depth z assumed to be uniform on the surface; λ_{Ag} is the attenuation length of the photoelectron coming from Ag; φ is the emission angle referred to the surface normal; and $I_{\mathrm{Ag}}{}^{0}$ is a constant depending on instrumental factors, angular asymmetry, and photoionization cross-section [34] which is the intensity measured from a standard Ag sample using the same experimental conditions. Equation (1) is an integral equation of the first kind and represents a prototype of ill-posed problems [39]. If a general algorithm involving regularization in addition to singular value decomposition (SVD) techniques [34] without any prior hypothesis on the shape of the concentration depth profile is used to extract the concentration depth profiles, $c_{Ag}(z)$, results of Fig. 7b are obtained for samples Ag/Ti= 1.49 (RT) and Ag/Ti = 0.2 (200 °C), which are those where significant variations of the Ag near surface concentration were found using GDOES. As can be seen from the results of Fig. 7b, the agreement between ARXPS results and GDOES results of Fig. 5 for the same samples is very good clearly confirming a silver enrichment in the first 2–3 nm of the sample surface. It should be pointed out that the regularization parameter used for solving the integral Eq. (1) was

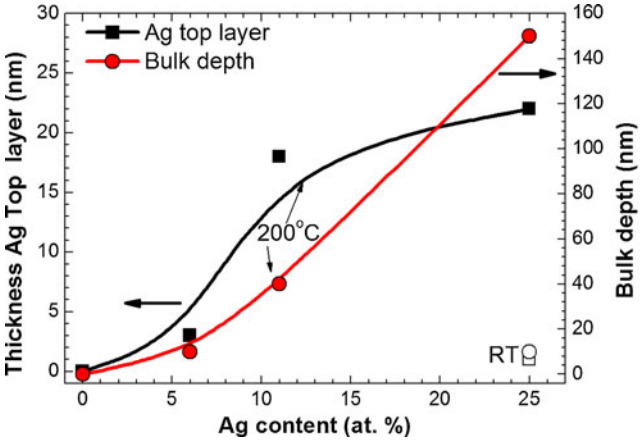

Fig. 6 Thickness of the Ag top layer (*closed squares*) and bulk depth (*closed circles*) as a function of the silver content in the samples prepared at 200 °C. The *open symbols* represent the values for the sample Ag/Ti = 1.49 deposited at room temperature. The *continuous lines* are plotted to guide the reader´s eye

chosen in the limit of stability in order to avoid meaningful solutions.

ARXPS measurement can be also used to provide further information on the surface morphology. This task can be accomplished assuming some hypothesis on the depth profile shape. In general, such depth profile would be dependent of some parameters that could be used as fitting parameters to minimize in Eq. (1) the differences between the measured intensities and the calculated ones using the proposed test depth profile. Therefore, assuming that Ag forms islands of height d and coverage θ, that is, $C_{Ag}(z)=1$ if $0 \le z \le d$ and $C_{Ag}(z)=0$ otherwise (this hypothesis is supported by SEM micrographs of Fig. 1), we should have

$$I_{\mathrm{Ag}}(\varphi) = I^{0}_{\mathrm{Ag}}\theta\left[1-\exp\left(-\frac{d}{\lambda\cos\varphi}\right)\right] \qquad (2)$$

where θ and d have to be used as fitting parameters to minimize the differences between the right side of Eq. (2), representing the measured intensities (concentrations), and the left side, representing the calculated ones. Obviously the limit case $\theta=1$ represents the results related to a step-like profile instead of islands.

We have used the ARXPS results of Fig. 7a to test both possibilities (1) step-like profile and (2) islands for the Ag distribution. Figure 8 shows the ARXPS results for the Ag/Ti=1.49 and Ag/Ti=0.2 (T) samples. Dashed lines in Fig. 8 represent the best fitting assuming $\theta=1$, that is, a step-like profile for the Ag concentration depth profile, whereas continuous lines represent the best-fitting assuming islands for the Ag distribution on the surface. The parameters leading to the best fit of the experimental data to an islands model are shown in Table 3.

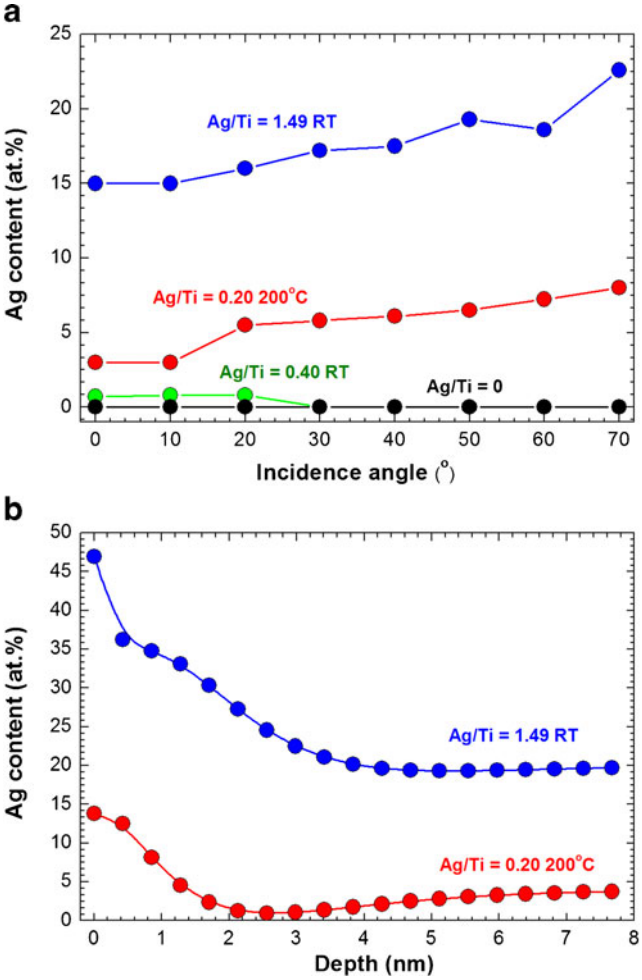

Fig. 7 **a** ARXPS data of samples Ag/Ti = 0, Ag/Ti = 0.20 (200 °C), Ag/Ti = 0.40 (RT), and Ag/Ti = 1.49 (RT). **b** Concentration depth profiles extracted from deconvolution of ARXPS data for samples Ag/Ti = 0.20 (200 °C) and Ag/Ti = 1.49 (RT)

As observed in Fig. 8, clearly a model of Ag islands on the surface is more appropriate to explain the experimental data than a step-like profile. In particular, for the sample with low silver content (Ag/Ti = 0.20) ARXPS provided a more detailed information than SEM with respect to the surface morphology of the samples.

Conclusions

From the above results, we can conclude that RBS, GDOES, and ARXPS are suitable and complementary techniques for in-depth and surface analysis of silver nanocluster segregation on Ag–TiCN coatings down to the nanometer level.

The depth profile analysis obtained by RBS for the samples with higher Ag content revealed that the Ag was not uniformly distributed along the coating thickness, being found that a top surface layer was formed, followed by a depletion zone both

for the samples deposited at RT and 200 °C, respectively. GDOES analysis were performed in the samples to obtain a more accurate depth resolution, confirming the RBS observation of the existence of a top surface rich in Ag followed by a depletion zone, for the coatings with higher silver contents independent of the deposition temperature. The silver top layer was estimated to be of 1 and 22 nm for samples deposited at room temperature and at 200 °C, respectively. The depletion zone was measured to be of 5 (room temperature) and 30 nm (200 °C). GDOES depth profiles also found a similar behavior for coatings deposited at 200 °C with lower silver content measuring the formation of an Ag-rich layer with a thickness of 3 nm and 18 nm, for coatings with Ag/Ti ratio of 0.20 and 0.40 GDOES analysis, respectively. Accordingly, the depletion zone depth was enhanced for higher Ag contents. The results obtained indicated that only the sample deposited at room temperature with the highest Ag content and those deposited at 200 °C showed the formation of an Ag-rich surface layer below which an Ag depletion zone of a few nanometers was formed. These observations were corroborated by ARXPS experiments and the subsequent modeling applying a general algorithm involving regularization to obtain the concentration depth profiles. This is attributed to the coalescence of Ag particles near the surface at the end of deposition process, which causes the growth of the Ag particles sited on the surface. As the surface particles grow at expense of the Ag clusters below the first nanometers under the surface, this creates a non-uniform Ag distribution in the first nanometers. Since the coalescence of Ag particles is due to the diffusion process, which is activated by the temperature, it was somehow expectable that the increase in the deposition temperature would promote the surface segregation. ARXPS measurements were used to provide further information on the surface morphology of the samples obtaining an excellent agreement with SEM observations when a growth model of silver islands with a height d=1.5 nm and coverage θ=0.20 was applied to the sample with Ag/Ti=1.49 and deposited at room temperature.

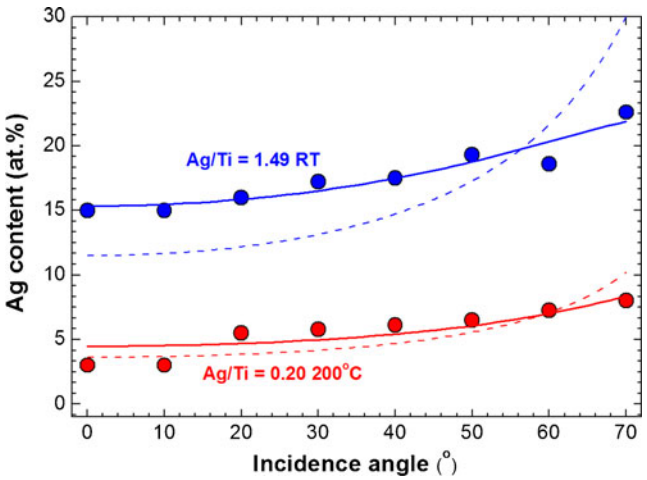

Fig. 8 Results of the parametric fitting of ARXPS data for samples Ag/Ti = 0.20 (200 °C) and Ag/Ti = 1.49(RT) (*closed circles*). The *dashed lines* correspond to the best fit obtained using a step-like model while *continuous lines* correspond to the best fit using an island model

Table 3 Results of the best-fit parameters islands (height d and coverage θ), obtained from parametric modeling of the ARXPS data

Sample	Film thickness d (nm)	Coverage θ
Ag/Ti = 1.49 RT	1.5	0.23
Ag/Ti = 0.2 200 °C	0.8	0.10

The production of Ag–TiCN coatings with small Ag clusters sited on the surface represents a promising structure for biomedical applications. However, it was found in previous studies that the presence of high Ag contents results in worse tribological performance. In this sense, coatings presented in this work with lower Ag content deposited at 200 °C represent a more challenging coating for antibacterial surfaces due to its higher surface area and, consequently, more likely to provide an enhanced silver ionization.

Acknowledgments This work was financially supported by the Spanish Ministry of Science and Innovation (projects FUNCOAT CSD2008-00023 and RyC2007-0026). This research is sponsored by FEDER funds through the program COMPETE "Programa Operacional Factores de Competitividade" and by national funds through FCT "Fundação para a Ciência e a Tecnologia", in the framework of the Strategic Projects PEST-C/FIS/UI607/2011, and PEST-C/EME/UI0285/2011 and under the project PTDC/CTM/102853/2008. The authors would like to acknowledge I. Caretti and R. Velasco for the fruitful discussions and the proofreading of the manuscript.

References

1. Hauert R (2003) Diam Rel Mater 12:583–589
2. Escudeiro A et al (2013) Thin Solid Films. doi:10.1016/j.tsf.2012.12.086
3. Liu C, Bi Q, Matthews A (2003) Surf Coat Technol 163–164:597–604
4. Serro AP et al (2009) Surf Coat Technol 203:3701–3707
5. Yildiz F, Yetimb AF, Alsaran A, Efeoglu I (2009) Wear 267:695–701
6. Oliveira C, Gonçalves L, Almeida BG, Tavares CJ, Carvalho S, Vaz F, Escobar Galindo R, Henriques M, Susano M, Oliveira R (2008) Surf Coat Technol 203:490–494
7. Oliveira C, Escobar Galindo R, Palacio C, Calderon S, Almeida BG, Henriques M, Espinosa A, Carvalho S (2011) Solid State Sci 13:95–100
8. Sánchez-López JC, Abad MD, Carvalho I, Escobar Galindo R, Benito N, Ribeiro S, Henriques M, Cavaleiro A, Carvalho S (2012) Surf Coat Technol 206:2192–2198
9. Mulligan CP, Blanchet TA, Galla D (2010) Wear 269:125–13110

10. Schierholz JM, Lucasj LJ, Rump A, Pulverer G (1998) J Hosp Infect 40:257–262
11. Kelly PJ, Li H, Benson PS, Whitehead KA, Verran J, Arnell RD, Iordanova I (2010) Surf Coat Technol 205:1606–16182
12. Morrison M, Buchanan R, Liaw P, Berry C, Brigmon R, Riester L, Abernathy H, Jin C, Narayan R (2006) Diam Rel Mater 15:138
13. Dowling DP, Betts AJ, Pope C, McConnell ML, Eloy R, Arnaud MN (2003) Surf Coat Technol 163–164:637–640
14. Hsieh JH, Tseng C, Chang YK, Chang SY, Wub W (2008) Surf Coat Technol 202:5586–5589
15. Cioffi N, Ditaranto N, Torsi L, Picca RA, Giglio E, Sabbatini L, Novello L, Tantillo G, Bleve-Zacheo T, Zambonin PG (2005) Anal Bioanal Chem 382:1912–191816
16. Li Q, Mahendra S, Lyon DY, Brunet L, Liga MV, Li D, Alvarez PJJ (2008) Water Res 42:4591–4602
17. Lok C, Ho CM, Chen R, He QY, Yu WY, Sun H, Tam PKH, Chiu JF, Che CM (2007) J Biol Inorg Chem 12:527–534
18. Morones J, Elechiguera JL, Cammacho A, Holt K, Kouri JB, Ramirez JT, Yacaman J (2005) Nanotechnol 16:2346–2353
19. Ferraris M, Perero S, Miola M, Ferraris S, Verné E, Morgiel J (2010) Mater Chem Phys 120:123–126
20. Escobar Galindo R, Gago R, Duday D, Palacio C (2010) Anal Bioanal Chem 396:2725–2740
21. Manninen NK et al (2011) J Phys D: Appl Phys 44:375501
22. Krzanowski JE, Endrino JL, Nainaparampil JJ, Zabinski JS (2004) J Mater Engin Perform 13(4):439
23. Adochite R, Munteanu D, Torrell M, Cunha L, Alves E, Barradas NP, Cavaleiro A, Riviere P, Bourhis E, Eyidi D, Vaz F (2012) Appl Surf Sci 258:4028–4034
24. Hu JJ, Muratore C, Voevodin AA (2007) Comp Sci Technol 67:336–347
25. Incerti L, Rotaa A, Valeri S, Miguel A, García JA, Rodríguez RJ, Osés J (2011) Vacuum 85:1108–1113
26. Clayton WB Jr, Chen QY (1995) Mater Lett 23:7–12
27. Climent-Font A, Pászti F, García G, Fernández-Jiménez MT, Agulló F (2004) Nucl Instrum Methods B 219:400–4
28. Kotai E (1994) Nucl Instrum Methods B 85:588–96
29. Mayer M (1997) SIMNRA User's Guide
30. Quentmeier A (1997) Sections 7.1 and 7.2. In: Payling R, Jones DG, Bengston A (eds) Glow discharge optical emission spectroscopy. Wiley, New York
31. Winchester R, Payling R (2004) Spectrochim. Acta Part B 59:607–666
32. Escobar Galindo R, Forniés E, Albella JM (2005) J Anal At Spectrom 20:1108–1115
33. Escobar Galindo R, Forniés E, Albella JM (2005) J Anal At Spectrom 20:1116–1120
34. Escobar Galindo R, Forniés E, Gago R, Albella JM (2007) J Anal At Spectrom 22:1512–1516
35. Arcos T, Oelhafen P, Aebi U, Hefti A, Duggelin M, Mathys D, Guggenheim R (2002) Vacuum 67:463–470
36. Niu F, Chang ITH, Dobson PJ, Cantor B (1997) Mater Sci Eng A226–228:161–167
37. Hofmann S (1991) Prog Surf Sci 36(1):35–87
38. CASA XPS software Ltd. v2.0 User's Manual www.casaxps.com. Accessed 10 January 2013
39. Palacio C, Ocón CP, Herrasti P, Díaz D, Arranz A (2003) J Electroanal Chem 545:53